Sparsity Weak Lensing 3-D Density Map Reconstruction

ABSTRACT

A new method is developed to reconstruct 3-D density contrast maps from photometric weak lensing shear measurements. The 3-D density contrast maps is modeled as a summation of basis atoms which are designed to represent the profiles of multi-scale NFW halos. The NFW atoms have 2-D multi-scale NFW surface density profiles on the transverse plane and 1-D Dirac delta functions in the line-of-sight direction. With the sparsity prior assumption, the density field is reconstructed using an oracle algorithm: adaptive lasso. Our method is tested with realistic simulations using HSC-like shape noise and photo-z uncertainties. Add descriptions on the outcomes of the test on the simulations.

1. INTRODUCTION

Light from distant galaxies is distorted by the intervening inhomogeneous density distribution along the line-of-sight due to the influence of gravity. As a result of the light distortion, the shapes of the background galaxies are coherently sheared. Such effect, which is known as weak lensing, imprints the information of foreground mass density distribution to the background galaxy images and offers a direct probe into the mass density distribution in our universe (see Kilbinger 2015; Mandelbaum 2018, for recent reviews).

Adopting the thin lens approximation, the expected shear measurements (γ) on distant galaxies are related to the foreground density contrast field (δ) through a linear transformation

$$\gamma = \mathbf{T}\delta, \qquad (1)$$

where $\mathbf{T}$ is used to denote the linear transformation operator which includes not only physical lensing effect but also observational systematic effects from the observation (e.g. pixelization and smoothing of shear field in transverse plane, photo-z uncertainties).

Several large scale surveys target to study the weak lensing effect at high precision level (e.g. HSC (Aihara et al. 2018), KIDS (de Jong et al. 2013), DES (The Dark Energy Survey Collaboration 2005), LSST (LSST Science Collaboration et al. 2009), Euclid (Laureijs et al. 2011), WFIRST (Spergel et al. 2015)).

The primary goal of most weak lensing surveys is to constrain the cosmology model through 2-point correlations. The studies include galaxy-galaxy lensing which cross correlating the shear field (γ) with the positions of foreground galaxies (Han et al. 2015; More et al. 2015; Prat et al. 2018), and cosmic shear which auto-correlates the shear measurements (Morrison et al. 2016; Troxel et al. 2018; Hikage et al. 2019; Hamana et al. 2020). Since shear is directly related to the matter distribu-

tion as shown in eq. (1), Galaxy-galaxy lensing probes into the correlation between the matter field and galaxy field, on the other hand, cosmic shear probes into the auto-correlation of matter field.

Reconstructions of density map from shear measurements also receive considerable interest. 2-D density map reconstruction which recover an integration of projected mass along the line-of-sight has been well studied within the community (Kaiser & Squires 1993; Lanusse et al. 2016) and applied to large scale surveys (Oguri et al. 2018; Chang et al. 2018; Jeffrey et al. 2018). However, the reconstruction of 3-D mass map is still a challenging task.

In order to fully reconstruct the 3-D mass density distribution (δ) from the tomographic shear observations (γ), the density contrast field is modeled as a summation of basis atoms in a model dictionary

$$\delta = \mathbf{\Phi}x, \qquad (2)$$

where $\mathbf{\Phi}$ is the transformation operator from the parameters in the dictionary space to the density contrast and x denotes the parameters. Simon et al. (2009) reconstruct the density field in Fourier space, which is equivalent to model the mass field with sinusoidial functions. On the other hand, Leonard et al. (2014) models the mass field with Starlets (Starck et al. 2015).

The model parameters are estimated through solving an optimization problem and the estimator is defined as

$$\hat{x} = \arg\min_{x} \left\{ \frac{1}{2} \left\| \Sigma^{-\frac{1}{2}}(\gamma - \mathbf{T}\mathbf{\Phi}x) \right\|_2^2 + \lambda C(x) \right\}, \quad (3)$$

where $\left\| \Sigma^{-\frac{1}{2}}(\gamma - \mathbf{T}\mathbf{\Phi}x) \right\|_2^2$ is the chi-square term[1] measuring the residuals between the prediction and the data,

---

[1] weighted by the inverse of the diagonal covariance matrix of error on the shear measurements (Σ).
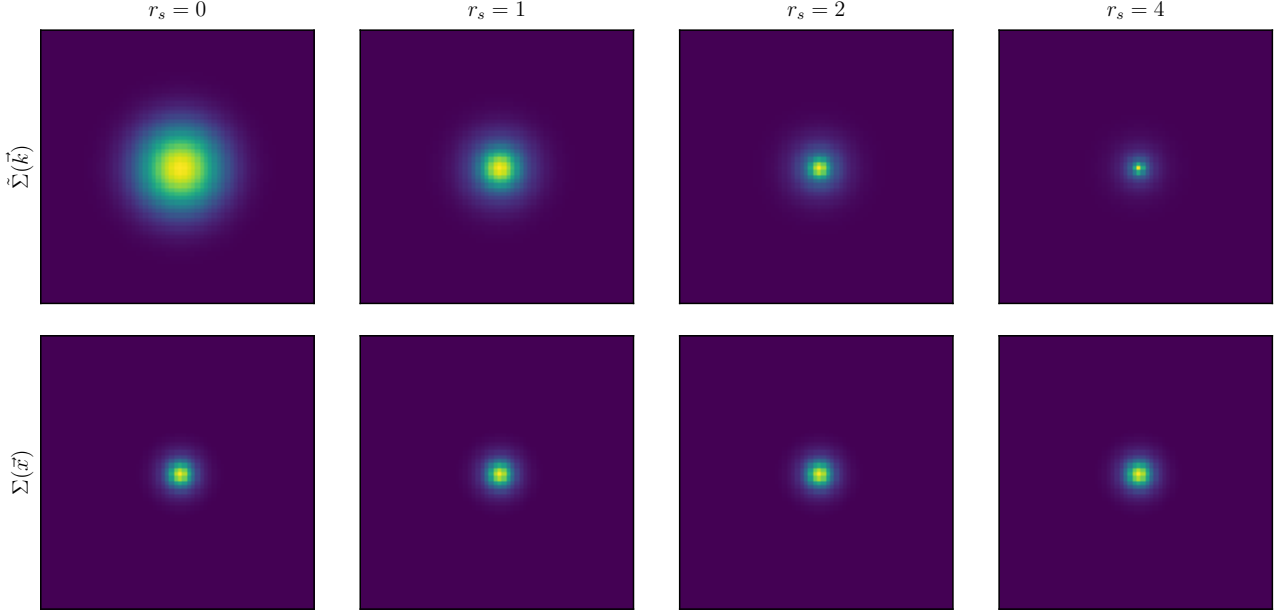
Figure 1. The smoothed basis atoms with different scale radius (r_s). The first row shows the smoothed basis atoms in Fourier space and the second row shows the smoothed basis atoms in Real space. The smoothing kernel is Gaussian with scale of 1.5 pixels.
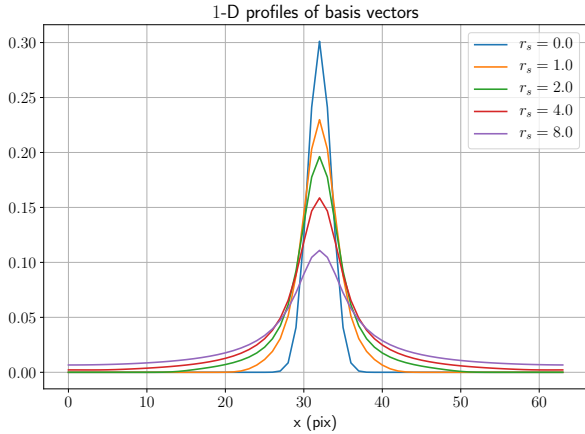

Figure 2. The 1-D slices for smoothed basis atoms at $x = 0$. The corresponding 2-D profiles are shown in Figure 1.

while $C(x)$ is the regularization term measuring the deviation of the estimation of the parameter (x) from the prior assumptions. Such estimation prefer the parameters that are able to describe the observations and also align with the prior assumptions. The regularization parameter λ adjusts the relative weight between the observations and prior assumptions in the optimization process.

Simon et al. (2009) propose to use the l^2 ridge regulation ($C = \|x\|_2^2$) to find a sparse solution in Fourier space. Oguri et al. (2018) apply the method of Simon et al. (2009) to the first year data of the Hyper Suprime-Cam Survey (Aihara et al. 2018). Why we use l^1 in this paper, what is the difference between l^1 and l^2.

Leonard et al. (2014) propose to use a derivative version of l^1 lasso regulation ($C = \|x\|_1^1$) to find a sparse solution in the Starlets dictionary space (Starck et al. 2015). However, the Starlets functions are not designed to model the profile of clumpy mass in the universe. Moreover, Leonard et al. (2014) apply a greedy coordinate descent algorithm, which selects the steepest coordinate in each iteration, find the minima of a non-convex loss function. However, the stability of the non-convex optimization has not been fully discussed.

N-body simulations have shown that the dark matter is distributed in halos connected by filaments, and the density profile of a single halo follows the NFW function (Navarro et al. 1997). We construct a dictionary which is composed of multi-scale NFW atoms. The multi-scale NFW atoms are used to model the profiles of halos. The atoms follow multi-scale surface density profiles of NFW functions (Takada & Jain 2003) on the transverse plane. The depth of halo is neglected (Leonard et al. 2014) since the resolution scale of the reconstruction in the line-of-sight direction is much larger than the halo scale. Therefore, the Dirac delta function is used to model the atoms' profile in the line-of-sight direction. With the prior assumption that the density contrast field is sparse in the dictionary space, the adaptive lasso regularization

(Zou 2006) is used to reconstruct a high signal-to-noise-ratio (SNR) density contrast field.

Comparing with Leonard et al. (2014), our dictionary is built up to describe the clumpy mass in the universe which has a clear physical motivation. Furthermore, the adaptive lasso algorithm is full convex and can be optimized with the FISTA algorithm (Beck & Teboulle 2009) without relying on any greedy coordinate descent approaches. The stability of this convex optimization has been well studied.

This paper is organized as follows. Section 2 proposes the new method for 3-D density map reconstruction. Section 3 introduces the realistic simulations we use to test the new method. Section 4 presents the results of our method on the simulations. Section 5 summarizes and discusses the future development of the method.

2. METHODOLOGY

We first review the lensing process in section 2.1. Then, we introduce the dictionary used to model the foreground density maps in section 2.2.

Subsequently, in section 2.3, we discuss several systematic effects from observations which include photo-z uncertainty (section 2.3.1), smoothing (section 2.3.2), masking(section 2.3.3), and pixelization (section 2.3.4).

Finally, we find the the sparse solution in section 2.4 using the adaptive lasso algorithm (Zou 2006) optimized with the FISTA alogrithm (Beck & Teboulle 2009).

2.1. Lensing

The lensing convergence map at the comoving distance χ_s caused by the foreground inhomogeneous density distribution at the comoving distance χ_l ($\chi_l < \chi_s$) along the line-of-sight is (Leonard et al. 2014)

$$\kappa(\vec{\theta}, \chi_s) = \frac{3H_0^2\Omega_M}{2c^2} \int_0^{\chi_s} d\chi_l \frac{\chi_l \chi_{sl}}{\chi_s} \frac{\delta(\vec{\theta}, \chi_l)}{a(\chi_l)}, \quad (4)$$

where $\delta = \rho(\vec{\theta}, \chi_l)/\bar{\rho} - 1$ is the density contrast at the position of lens, H_0 is the Hubble parameter, Ω_M is the matter density parameter, c is the speed of light, and $a(\chi_l)$ is the scale parameter at the lens position.

Substitute comoving distance (χ) with redshift (z)

$$\kappa(\vec{\theta}, z_s) = \int_0^{z_s} dz_l K(z_l, z_s)\delta(\vec{\theta}, z_l). \quad (5)$$

where $K(z_l, z_s)$ is the lensing kernel defined as

$$K(z_l, z_s) = \begin{cases} \frac{3H_0\Omega_M}{2c} \frac{\chi_l\chi_{sl}(1+z_l)}{\chi_s E(z_l)} & (z_s > z_l), \\ 0 & (z_s \le z_l). \end{cases} \quad (6)$$

As shown in Kaiser & Squires (1993), the shear distortion is related to the kappa field at the redshift plane as

$$\gamma_L(\vec{\theta}, z_s) = \int d^2\theta' D(\vec{\theta} - \vec{\theta'})\kappa(\vec{\theta'}, z_s), \quad (7)$$

where

$$D(\vec{\theta}) = -\frac{1}{\pi}(\theta_1 - i\theta_2)^{-2}. \quad (8)$$

Here we denote the physical shear distortions as γ_L and we note that the observed shear measurements are the physical shear distortions influenced by systematics which will be discussed in the following subsections.

Combining equation (5) with equation (7), the physical shear signal is derived as

$$\gamma_L(\vec{\theta}, z_s) = \int_0^{z_s} dz_l K(z_l, z_s) \int d^2\theta' \vec{D}(\vec{\theta} - \vec{\theta'})\delta(\vec{\theta'}, z_l). \quad (9)$$

To simplify the expression, we define the lensing transform operator as

$$\mathbf{Q} = \int_0^{z_s} dz_l K(z_l, z_s) \int d^2\theta' \vec{D}(\vec{\theta} - \vec{\theta'}), \quad (10)$$

and eq. (9) is simplified to

$$\gamma_L = \mathbf{Q}\delta. \quad (11)$$

2.2. Dictionary

The density contrast field is modeled as a summation of basis atoms in the dictionary space $\{\phi_0, \phi_1, ...\phi_N\}$.

$$\delta(\vec{r}) = \sum_{s=0}^{N} \int d^3r' \phi_s(\vec{r} - \vec{r'})x_s(\vec{r'}), \quad (12)$$

where $\phi_s(\vec{r})$ is the basis vector of the dictionary space, and x_s is the corresponding projection coefficients of the density contrast field onto the basis vectors.

These basis vectors are composed of multi-scale NFW atoms $\{\phi_1, .., \phi_N\}$ and point mass atoms $\{\phi_0\}$. ϕ_0 is a 3-D Dirac delta function

$$\phi_0(\vec{r}) = \delta_D(\theta_1)\delta_D(\theta_2)\delta_D(z). \quad (13)$$

on the transverse plane, the NFW atoms ($\{\phi_1, ..., \phi_N\}$) follow surface density profiles of NFW halos (Takada & Jain 2003) with scale radius θ_α and truncation radius $c\theta_\alpha$, where c is known as concentration of NFW halo. As the scale of halo is much less than the reachable redshift resolution, we neglect the depth of halo on the line-of-sight direction and set the profiles of NFW atoms in the line-of-sight direction to 1-D Dirac delta functions (Leonard et al. 2014). The NFW atoms are expressed as

$$\phi_\alpha(\vec{r}) = \frac{f}{2\pi\theta_\alpha^2} F(|\vec{\theta}|/\theta_\alpha)\delta_D(z), \quad (s = 1..N) \quad (14)$$

where

$$F(x) = \begin{cases} -\frac{\sqrt{c^2-x^2}}{(1-x^2)(1+c)} + \frac{\operatorname{arccosh}\left(\frac{x^2+c}{x(1+c)}\right)}{(1-x^2)^{3/2}} & (x < 1), \\ \frac{\sqrt{c^2-1}}{3(1+c)}\left(1 + \frac{1}{c+1}\right) & (x = 1), \\ -\frac{\sqrt{c^2-x^2}}{(1-x^2)(1+c)} + \frac{\arccos\left(\frac{x^2+c}{x(1+c)}\right)}{(x^2-1)^{3/2}} & (1 < x \le c), \\ 0 & (x > c). \end{cases}$$

(15)

$f = 1/[\ln(1+c) - c/(1+c)]$. In this work, we fix $c = 9$ for NFW atoms in different scale frames.

To simplify the notation, we define the projection parameters as a column vector: $x = \begin{pmatrix} x_0 \\ x_1 \\ ... \\ x_N \end{pmatrix}$, and the dictionary transform operator as a row vector:

$$\mathbf{\Phi} = \left(\int d^3r\phi_0(\vec{r}) \; \int d^3r\phi_1(\vec{r}) \; ... \; \int d^3r\phi_N(\vec{r}) \right).$$

(16)

We substitute eq. (12) into eq.(9)

$$\gamma_L = \mathbf{Q}\mathbf{\Phi}x.$$

(17)

Our prior assumption is that the mass density field is sparse in the dictionary space and we will conduct adaptive lasso (Zou 2006) to find a sparse solution of the mass reconstruction problem in the dictionary space.

We note that the shear measurements are deviated from the physical shear prediction due to the systematics from observations. The influence of systematics is carefully studied and added to the forward modeling in the following subsections.

2.3. Systematics

2.3.1. Photo-z Uncertainty

Since the photometric redshifts of source galaxies in the current large scale survey are estimated with a limited number of photometric bands, the estimated redshifts of galaxies suffer from large uncertainties. Such uncertainties smear the structure along the line-of-sight direction since a galaxy with a best fit photo-z estimation of z_s has a possibility of being actually located at redshift z. Such probability is denoted as $P(z|z_s)$ and the expected shear distortion on this galaxy is

$$\gamma_L(\vec{\theta}, z_s) \to \int dz_s P(z|z_s)\gamma_L(\vec{\theta}, z_s).$$

(18)

With the definition of photo-z smearing operator

$$\mathbf{P} = \int dz_s P(z|z_s),$$

(19)

the photo-z uncertainties changes the shear as $\gamma_L \to \mathbf{Q}\gamma_L$.
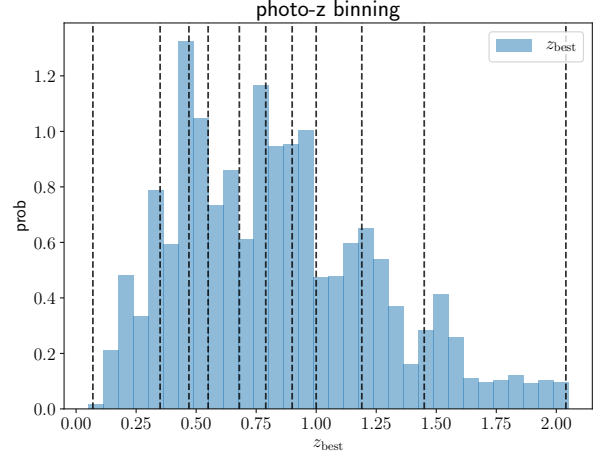

Figure 3. The source galaxies are binned into 10 redshift bins according to their mlz best photo-z estimation. The blue histogram is the number distribution of the best photo-z estimation. The vertical dashed lines are the bounds of bins. The galaxies are evenly distributed in each bins.

2.3.2. Smoothing

The observed galaxies have random irregular (unequally-spaced) spacial distribution. To benefit the computational speed, we smooth the shear measurements from galaxy shapes and pixelise the smoothed measurements onto regular grids.

The smoothing is conducted by convolving the measurements with a smoothing kernel

$$\hat{\gamma} = \frac{\sum_i W(\vec{\theta} - \vec{\theta}_i, z - z_i)e_i}{\sum_i R_i W(\vec{\theta} - \vec{\theta}_i, z - z_i)},$$

(20)

where $W(\vec{\theta}, z)$ is a 3-D smoothing kernel. e_i, R_i, z_i and θ_i are the ellipticity, response, reshift, and transverse position of the 'i-th' galaxy in the galaxy catalog.

$W(\vec{\theta}, z)$ can be decomposed into a transverse component $W_T(\vec{\theta})$ and a line-of-sight component $W_\times(z)$

$$W(\vec{\theta}, z) = W_T(\vec{\theta})W_\times(z).$$

(21)

In this paper, we set

$$W_T(\vec{\theta}) = \frac{1}{2\pi\beta^2}\exp\left(-\frac{|\vec{\theta}|}{2\beta^2}\right),$$

$$W_\times(z) = \begin{cases} 1/\Delta z & (|z| < \Delta z/2), \\ 0 & else. \end{cases}$$

(22)

With the approximation that the density of galaxy number vary slowly on the smoothing scale and the fact that $\int d^3r W(\vec{r}) = 1$, the smoothing operator is defined

as

$$\mathbf{W} = \int d^3r' W(\vec{r} - \vec{r'}), \tag{23}$$

and the relation between shear signal and projections in the dictionary space is $\gamma_L \to \mathbf{W}\gamma_L$.

2.3.3. Masking

In the forward modeling, normally the shear field has its prediction on any points within a regular region. However, in real observations, the boundary of the survey, where shear measruements is recorded, is always irregular. Moreover, there are also many regions are masked out due to the existence of neighboring bright stars or bad pixels as bight stars and bad pixels are likely to bias the shape measurements. Therefore, it is necessary to add an mask on the shear field prediction in the forward modeling to match the prediction with realistic observations. The mask changes the shear prediction as follows

$$\gamma_L(\vec{\theta}, z) \to M(\vec{\theta}, z)\gamma_L(\vec{\theta}, z), \tag{24}$$

$M(\vec{\theta}, z_s)$ is the masking function which is defined as

$$M(\vec{r}) = \begin{cases} 0 & \vec{r} \text{ resides in masked area} \\ 1 & \text{else.} \end{cases} \tag{25}$$

We define the masking operator as

$$\mathbf{M} = \int d^3r' M(\vec{r'})\delta_D(\vec{r} - \vec{r'}), \tag{26}$$

where $\delta_D(\vec{r})$ is 3-D Dirac delta function. The shear is influenced by the masking through $\gamma_L \to \mathbf{M}\gamma_L$.

The final observed shear field, taking into account all of the aforementioned systematics from observations, is

$$\gamma = \mathbf{MWPQ\Phi}x. \tag{27}$$

For simplicity, we denote $\mathbf{A} = \mathbf{MWPQ\Phi}$ and eq. (27) is written as

$$\gamma = \mathbf{A}x. \tag{28}$$

2.3.4. Pixelization

We pixelize the smoothed shear field into a $N_\theta \times N_\theta \times N_s$ grid, where N_θ is the number of pixels of two orthogonal axes of the transverse plane and N_s is the number of pixels of the line-of-sight axis. γ_α is used to denote the value recorded on pixel with index α, where $\alpha = 1, ..., N_\theta \times N_\theta \times N_s$. The grid on the transverse plan is equally spaced, therefore Fast Fourier Transform (FFT) can be used to boost the speed of linear operation on the transverse plan.

Similarly, we pixelize each scale frame of the parameter x into a $N_\theta \times N_\theta \times N_l$ grid. The pixelization of the
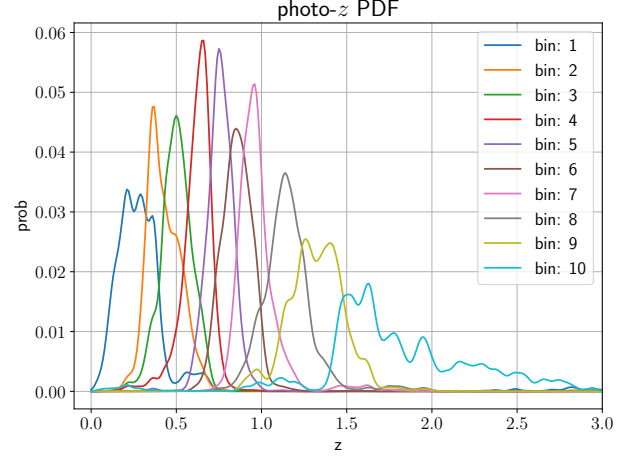

Figure 4. The PDF of photo-z error for 10 source redshift bins.

parameter x on the transverse plan for each scale frame is exactly the same as the pixelization of the smoothed shear field on the transverse plane. N_l is the pixel number of the line-of-sight axis. x_β is used to denote the element of parameter vector x with index β, where $\beta = 1, ..., N_\theta \times N_\theta \times N_l \times N$. The elements of the forward transform matrix $\mathbf{A}$ is denoted as $A_{\alpha\beta}$.

We term the column vectors of the transform matrix $\mathbf{A}$ as the effective basis vectors. We note that the effective basis vectors have different l^2 norm. The l^2 norm of the $i'th$ column vectors of the effective basis vectors are $\mathcal{N}_i = \sum_\alpha A_{i\alpha}A_{i\alpha}$. Before solving the density map inversion problem, we normalize the column vectors of the transform matrix through

$$\begin{aligned} A'_{\alpha\beta} &= A_{\alpha\beta}/\mathcal{N}_\alpha^{\frac{1}{2}}, \\ x'_\beta &= x_\beta \mathcal{N}_\beta^{\frac{1}{2}}. \end{aligned} \tag{29}$$

2.4. Density map reversion

2.4.1. Adaptive lasso

The lasso algorithm uses l^1 penalty as the regularization term and the estimator is defined as

$$\hat{x'} = \arg\min_x \left\{ \frac{1}{2}\left\|\Sigma^{-\frac{1}{2}}(\gamma - \mathbf{A}'x')\right\|_2^2 + \lambda\|x'\|_1^1 \right\}, \tag{30}$$

where $\|\cdot\|_1$ and $\|\cdot\|_2$ refer to the l^1 norm and l^2 norm, respectively. The l^p norm is defined as

$$\|x'\|_p = \left(\sum_i |x'|_i^p\right)^{\frac{1}{p}}. \tag{31}$$

Given that the parameters to measure is sparse in the parameter space, the lasso algorithm can select the parameters which are relevant to the measurements and

simultaneously estimate the value of the selected parameters. However, it has been shown by Zou (2006) that when the column vectors of $\mathbf{A}'$ are highly correlated, lasso cannot select the related parameters from the parameter space consistently. Moreover, the estimated parameters are biased due to the shrinkage process in the lasso regression.

Zou (2006) proposes the adaptive lasso algorithm which uses adaptive weights to penalize different coefficients in the l^1 penalty. The addaptive lasso algorithm is a two-steps process. First, Lasso estimation is performed in the first step and achieve a preliminary lasso estimation of parameter $(\hat{x'}^{\mathrm{lasso}})$. In the second step, the lasso estimation is used to weight the penalization on the parameters. With the definition of the adaptive lasso weight

$$\hat{w} = \frac{1}{\left|\hat{x'}^{\mathrm{lasso}}\right|^{\tau}}, \tag{32}$$

here we set the hyper-parameter τ to 2, the adaptive lasso estimator is expressed as

$$\hat{x}' = \arg\min_{x'} \left\{ \frac{1}{2} \left\| \Sigma^{-\frac{1}{2}} (\gamma - \mathbf{A}'x') \right\|_2^2 + \hat{w}\lambda \|x'\|_1^1 \right\}. \tag{33}$$

The loss function can be rewritten with Einstein notation

$$L(x') = \frac{1}{2}(\Sigma^{-1})_{\alpha\beta}(\gamma_\alpha^* - A_{\alpha i}'^* x_i')(\gamma_\beta - A_{\beta j}' x_j') \\ + \lambda \hat{w}_\beta \left| x_\beta' \right|. \tag{34}$$

To simplify the notification, we define the quadruple term in the loss function as $G(x')$:

$$G(x') = \frac{1}{2}\Sigma_{\alpha\beta}^{-1}(\gamma_\alpha^* - A_{\alpha i}'^* x_i')(\gamma_\beta - A_{\beta j}' x_j'). \tag{35}$$

2.4.2. FISTA

In this work, we apply the Fast Iterative Soft Thresholding Alorithm (FISTA) of Beck & Teboulle (2009) to solve the adaptive lasso estimator.

The parameter vector is initialized as $x^{(1)} = 0$. According to the FISTA algorithm, we iteratively update the elements of the parameter vector (x). In the n'th iteration, a temporary update is first calcualted as

$$x_i'^{(n+1)} = \mathrm{ST}_\lambda \left(x_i'^{(n)} - \mu \partial_i G(x'^{(n)}) \right), \tag{36}$$

where ST is the soft thresholding function defined as

$$\mathrm{ST}_\lambda \left(x' \right) = \mathrm{sign}(x') \max \left(|x'| - \lambda, 0 \right). \tag{37}$$

μ is the step size of the gradient descent iteration. $\partial_i G(x'^{(n)})$ refers to the i'th element of the gradient vector of G at point $x'^{(n)}$

$$\partial_i G(x'^{(n)}) = \Sigma_{\alpha\beta}^{-1} \mathrm{Re} \left(A_{\alpha i}'^* (\gamma_\beta - A_{\beta j}' x_j') \right), \tag{38}$$

where $\mathrm{Re}(\bullet)$ is the function returns the real part of the input function. The FISTA algorithm requires an additional step amounting to a weighted average between $x'^{(n+1)}$ and $x'^{(n)}$:

$$t^{(n+1)} = \frac{1 + \sqrt{1 + 4(t^{(n)})^2}}{2}, \\ x_{n+1}' \leftarrow x'^{(x+1)} + \frac{t^{(n)} - 1}{t^{(n+1)}}(x'^{(n+1)} - x'^{(n)}), \tag{39}$$

where the relative weight is initialized as $t^{(1)} = 1$.

Note that the FISTA algorithm coverges as long as the gradient descent step size μ satisfies

$$0 < \mu < \frac{1}{\left\| \mathbf{A}^\dagger \Sigma^{-1} \mathbf{A} \right\|}, \tag{40}$$

where $\left\| \mathbf{A}^\dagger \Sigma^{-1} \mathbf{A} \right\|$ refers to the spectrum norm of the matrix $\mathbf{A}^\dagger \Sigma^{-1} \mathbf{A}$. The spectral norm is estimated using random vectors. We simulate large number of random vectors with l^2 norms equal one with different realizations. Then, the matrix $\mathbf{A}^\dagger \Sigma^{-1} \mathbf{A}$ is applied to each random vector and get a corresponding transformed random vector. The spectral norm of the matrix $\mathbf{A}^\dagger \Sigma^{-1} \mathbf{A}$ is the maximum l^2 norm of the transformed vectors.

2.4.3. The Algorithm

The algorithm is described in Algorithm 2.4.3.

Algorithm Our Algorithm

Input: γ: Pixelized complex 3-D array of shear
Output: δ: 3-D array of density contrast
1: Normalize column vectors of $\mathbf{A}$
2: Estimate step size μ and Σ
3: **Initialization:**
4: $x'^{(1)} = 0$
5: $\hat{w} = 1$
6: $t^{(1)} = 1, i = 1, j = 1$
7: **while** $j \leq 2$ **do**
8:     **while** $i \leq N_{\mathrm{iter}}$ **do**
9:         $x_i'^{(n+1)} = \mathrm{ST}_{\hat{w}\lambda} \left(x_i'^{(n)} - \mu \partial_i G(x'^{(n)}) \right)$
10:         $t^{(n+1)} = \frac{1 + \sqrt{1 + 4(t^{(n)})^2}}{2}$
11:         $x_{n+1}' \leftarrow x'^{(x+1)} + \frac{t^{(n)} - 1}{t^{(n+1)}}(x'^{(n+1)} - x'^{(n)})$
12:     **end while**
13:     **Reinitialization:**
14:     $\hat{w} \leftarrow \left| \hat{x'}^{\mathrm{lasso}} \right|^{-2}$
15:     $\hat{x}'^{(1)} \leftarrow x'^{(N_{\mathrm{iter}})}$
16:     $t^{(1)} \leftarrow 1, i \leftarrow 1$
17: **end while**
18: $\delta = \mathbf{\Phi} \mathcal{N}^{-\frac{1}{2}} x'^{(N_{\mathrm{iter}})}$

---

3. SIMULATION

This section simulates lensing shear fields induced by a group of dark matter halos with various halo masses and redshifts. Then the shear distortions are applied to HSC mock catalogs with different realizations of HSC-like shape noises and photo-z uncertainties.

The ΛCDM cosmology used for the simulations is from the best fitting result of the final full-mission Planck observation of the cosmic microwave background (CMB) with $H_0 = 67.4$ km s^{-1}Mpc^{-1} $\Omega_M = 0.315$, $\Omega_\Lambda = 0.685$ (Planck Collaboration et al. 2020).

3.1. Weak Lensing Fields

We sample halos in two dimensional (mass, redshift) plane. The two dimensional plane is divided into eight redshift bins times eight mass bins. The input redshifts and masses are shifted by random values for each halo, respectively.

We simulate weak lensing shear fields of NFW halos according to Takada & Jain (2003) We assume a dependency of the concentration on the mass and the redshift of a halo Ragagnin et al. (2019, equation (2))

$$c_h = 6.02 \times (\frac{M_{200}}{10^{13}M_\odot})^{-0.12}(\frac{1.47}{1. + z_h})^{0.16}. \quad (41)$$

3.2. HSC mock Catalog
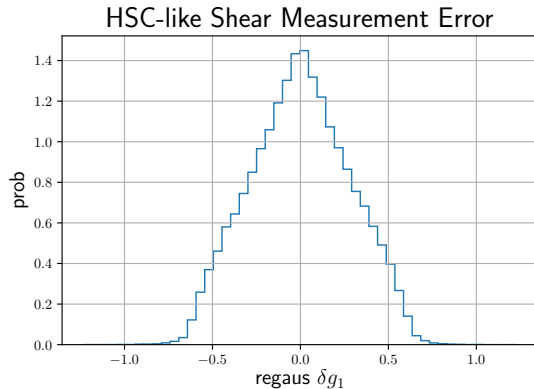
Figure 5. HSC-like measurement error on the first component of shear (g_1).

For each galaxy, we randomly assign its redshift following the MLZ photo-z probability distribution function (Tanaka et al. 2018) of the galaxy. The shear values are obtained from the all-sky weak lensing maps at two adjacent redshift slices with linearly interpolation.

4. RESULTS

4.1. Detection

4.2. Redshift

4.3. Density Map

5. SUMMARY

We develope a novel method to reconstruct 3-D density contrast maps from photometric weak lensing shear measurements. Our method models 3-D density contrast maps as a summation of NFW atoms with multiple comoving radius and point mass atoms in the 3-D space binned with photometric redshift. The NFW atoms are used to model the mass in isolated halos and the point mass atoms are used to model the structures close to the resolution limit of the reconstruction.

With the prior assumption that the basis atoms sparsely distributes in the 3-D space, the density field is reconstructed using the adaptive lasso algorithm (Zou 2006) which has the oracle properties.

The method is tested with realistic simulations using HSC-like shape noise and photo-z uncertainties.
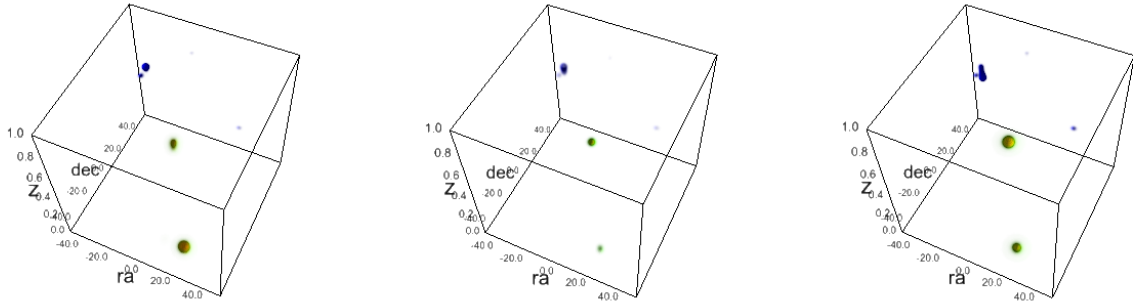
Figure 6. The density map reconstructed for a halo with mass=$3.16 \times 10^{1}4M_{\odot}/h$, $z = 0.51$. The left panel shows the results with $\tau = 0.10$, the middle panel is the result for $\tau = 0.15$, the right panel is for $\tau = 0.20$.
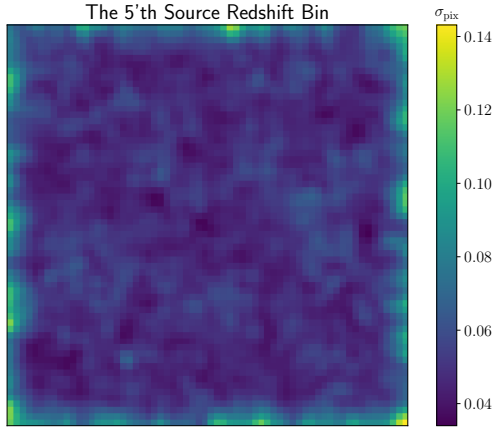
Figure 7. The standard deviation map of shear measurement error for the fifth source bin ($0.69 \leq z < 0.80$).
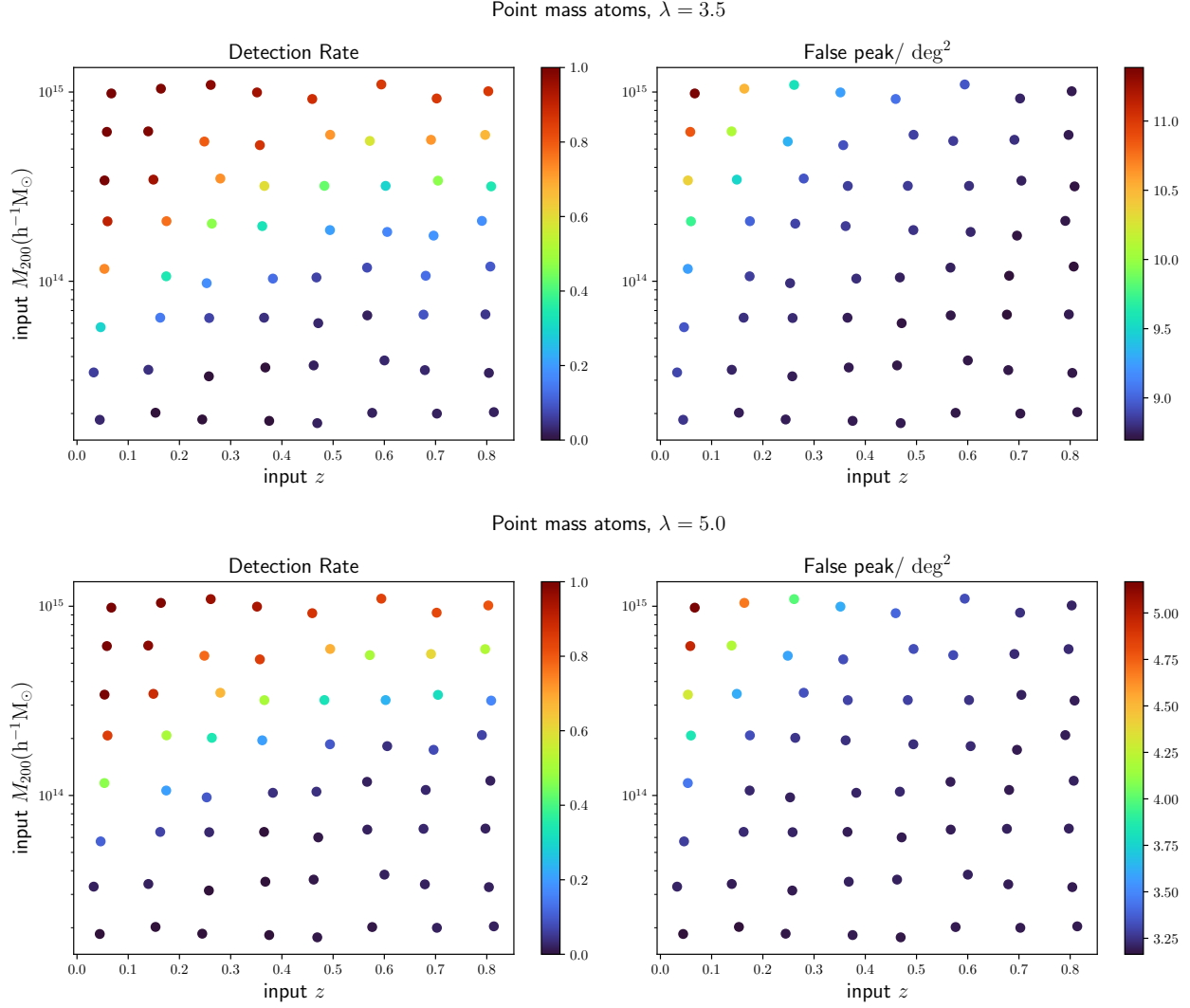
Figure 8. The upper panels show the detection rate and false peak per square degree for mass map reconstruction with point mass atoms and $\lambda = 3.5$. The low panels show the results for $\lambda = 5.0$.
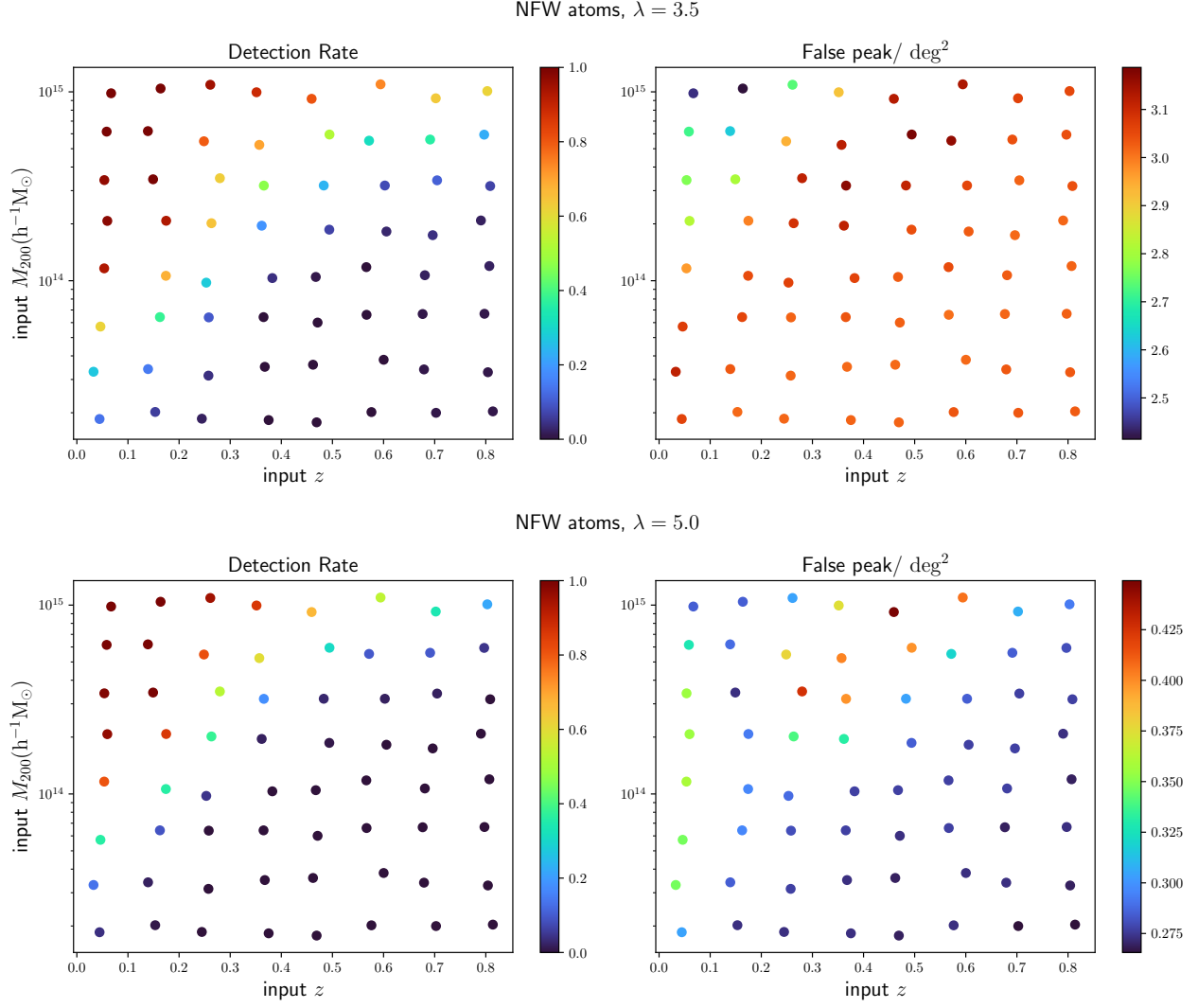
Figure 9. The upper panels show the detection rate and false peak per square degree for mass map reconstruction with NFW atoms and $\lambda = 3.5$. The low panels show the results for $\lambda = 5.0$.
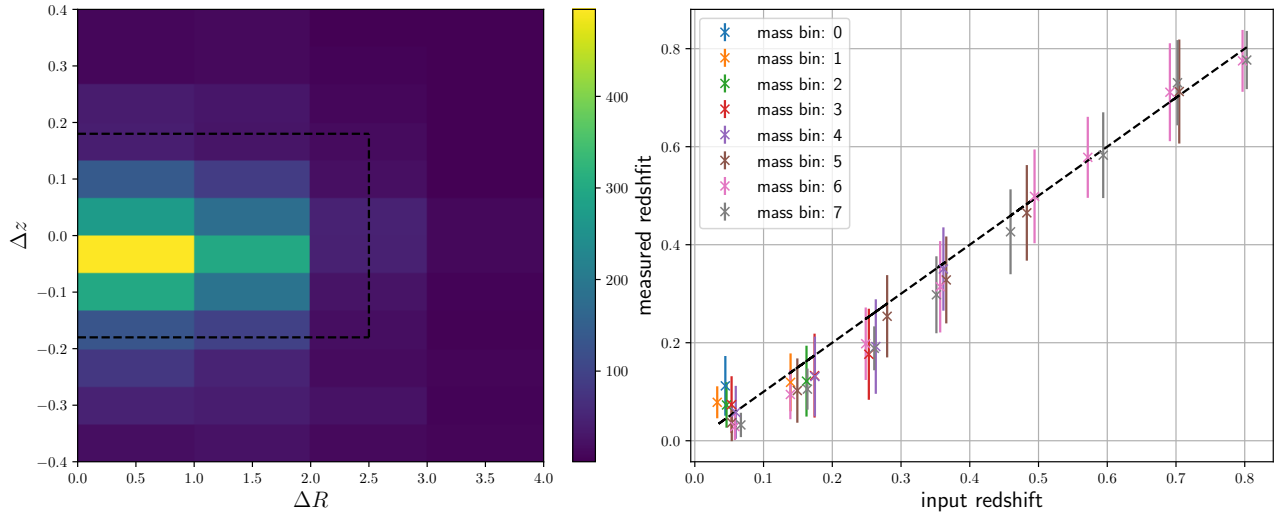
Figure 10. The left panel shows the stacked distribution of deviations of detected peak positions from the centers of the corresponding input halos. The x-axis is for the deviated distance in the transverse plane and the y-axis is for the deviation of the redshift. The peaks inside the dashed black box are regarded as true detections. The right panel focus on the deviation of detected peaks in the line-of-sight direction. The x-axis shows the input redshifts and the y-axis is the redshift of the detected peak. The cross symbols show the average redshift of detected peak for halos with different input redshift and mass and the error-bars are the scatter of the corresponding peak redshifts. All of the results in this figure are based on the NFW atoms.
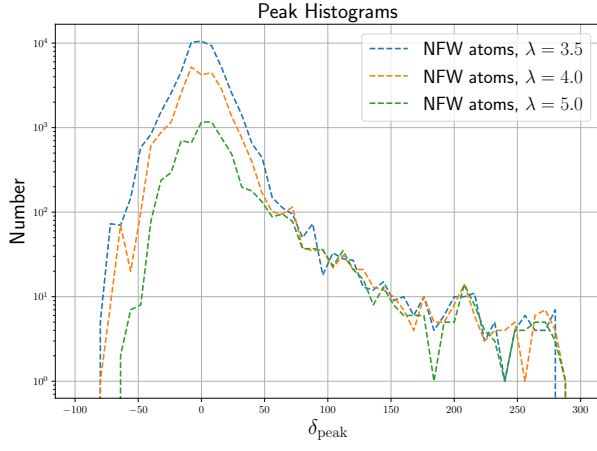
Figure 11. The histograms of detected peak values for all of the halo and error realizations. The dotted lines with different colors are for the results of reconstruction with NFW atoms dictionary penalized with different regularization parameter λ.

REFERENCES

Aihara, H., Armstrong, R., Bickerton, S., et al. 2018, PASJ, 70, S8, doi: 10.1093/pasj/psx081

Beck, A., & Teboulle, M. 2009, SIAM Journal on Imaging Sciences, 2, 183

Chang, C., Pujol, A., Mawdsley, B., et al. 2018, MNRAS, 475, 3165, doi: 10.1093/mnras/stx3363

de Jong, J. T. A., Kuijken, K., Applegate, D., et al. 2013, The Messenger, 154, 44

Hamana, T., Shirasaki, M., Miyazaki, S., et al. 2020, PASJ, 72, 16, doi: 10.1093/pasj/psz138

Han, J., Eke, V. R., Frenk, C. S., et al. 2015, MNRAS, 446, 1356, doi: 10.1093/mnras/stu2178

Hikage, C., Oguri, M., Hamana, T., et al. 2019, PASJ, 71, 43, doi: 10.1093/pasj/psz010

Jeffrey, N., Abdalla, F. B., Lahav, O., et al. 2018, MNRAS, 479, 2871, doi: 10.1093/mnras/sty1252

Kaiser, N., & Squires, G. 1993, pj, 404, 441, doi: 10.1086/172297

Kilbinger, M. 2015, Reports on Progress in Physics, 78, 086901, doi: 10.1088/0034-4885/78/8/086901

Lanusse, F., Starck, J. L., Leonard, A., & Pires, S. 2016, ap, 591, A2, doi: 10.1051/0004-6361/201628278

Laureijs, R., Amiaux, J., Arduini, S., et al. 2011, ArXiv e-prints. https://arxiv.org/abs/1110.3193

Leonard, A., Lanusse, F., & Starck, J.-L. 2014, MNRAS, 440, 1281, doi: 10.1093/mnras/stu273

LSST Science Collaboration, Abell, P. A., Allison, J., et al. 2009, ArXiv e-prints. https://arxiv.org/abs/0912.0201

Mandelbaum, R. 2018, ARA&A, 56, 393, doi: 10.1146/annurev-astro-081817-051928

More, S., Miyatake, H., Mandelbaum, R., et al. 2015, The Astrophysical Journal, 806, 2, doi: 10.1088/0004-637x/806/1/2

Morrison, C. B., Klaes, D., van den Busch, J. L., et al. 2016, Monthly Notices of the Royal Astronomical Society, 465, 1454, doi: 10.1093/mnras/stw2805

Navarro, J. F., Frenk, C. S., & White, S. D. M. 1997, pj, 490, 493, doi: 10.1086/304888

Oguri, M., Miyazaki, S., Hikage, C., et al. 2018, PASJ, 70, S26, doi: 10.1093/pasj/psx070

Planck Collaboration, Aghanim, N., Akrami, Y., et al. 2020, ap, 641, A6, doi: 10.1051/0004-6361/201833910

Prat, J., Sánchez, C., Fang, Y., et al. 2018, Phys. Rev. D, 98, 042005, doi: 10.1103/PhysRevD.98.042005

Ragagnin, A., Dolag, K., Moscardini, L., Biviano, A., & D'Onofrio, M. 2019, MNRAS, 486, 4001, doi: 10.1093/mnras/stz1103

Simon, P., Taylor, A. N., & Hartlap, J. 2009, MNRAS, 399, 48, doi: 10.1111/j.1365-2966.2009.15246.x

Spergel, D., Gehrels, N., Baltay, C., et al. 2015, ArXiv e-prints. https://arxiv.org/abs/1503.03757

Starck, J., Murtagh, F., & Bertero, M. 2015, Starlet transform in astronomical data processing, ed. O. Scherzer, Vol. 1 (United States: Springer New York), 2053–2098

Takada, M., & Jain, B. 2003, MNRAS, 340, 580, doi: 10.1046/j.1365-8711.2003.06321.x

Tanaka, M., Coupon, J., Hsieh, B.-C., et al. 2018, Publications of the Astronomical Society of Japan, 70, S9, doi: 10.1093/pasj/psx077

The Dark Energy Survey Collaboration. 2005, ArXiv Astrophysics e-prints

Troxel, M. A., MacCrann, N., Zuntz, J., et al. 2018, Phys. Rev. D, 98, 043528, doi: 10.1103/PhysRevD.98.043528

Zou, H. 2006, Journal of the American Statistical Association, 101, 1418, doi: 10.1198/016214506000000735

APPENDIX